In situ monitoring and 3D geomechanical numerical modelling to evaluate seismic and aseismic rock deformation in response to deep mining

Francesca de Santis, Vincent Renaud, Yann Gunzburger, Jannes Kinscher, Pascal Bernard, Isabelle Contrucci

In situ monitoring and 3D geomechanical numerical modelling to evaluate seismic and aseismic rock deformation in response to deep mining.

Francesca De Santis (1), e-mail: francesca.de-santis@ineris.fr

Vincent Renaud (1), e-mail: vincent.renaud@ineris.fr

Yann Gunzburger (2), e-mail: yann.gunzburger@univ-lorraine.fr

Jannes Kinscher (1), e-mail: jannes-l.kinscher@ineris.fr

Pascal Bernard (3), e-mail: bernard@ipgp.fr

Isabelle Contrucci (1), e-mail: isabelle.contrucci@ineris.fr

(1) Institut National de l'Environnement Industriel et des Risques (Ineris), Campus ARTEM CS14234, 92 rue du Sergent Blandan, 54042 Nancy Cedex, France.

(2) Université de Lorraine – CNRS, GeoRessources lab., Mines Nancy, Campus ARTEM, BP 14234, F-54 042 Nancy cédex, France.

(3) Equipe de Sismologie, Institut de Physique du Globe de Paris, 1, rue Jussieu, 75238 Paris Cedex 05, France

Corresponding author: Francesca De Santis. Address: Ineris, Campus ARTEM CS14234, 92 rue du Sergent Blandan, 54042 Nancy Cedex, France. E-mail: francesca.de-santis@ineris.fr. Phone: +33 3 54 40 66 18

Abstract

19

20   In this work we investigated seismic and aseismic rock mass behaviors in response to deep

21 underground mining. For this purpose, an area under production of the metal mine of Garpenberg

22 (Sweden) was instrumented with a geophysical and geotechnical monitoring network. In situ

23 monitoring data were analyzed and interpreted considering mining operations and the local

24 geological setting. In addition, a 3D elasto-plastic numerical model was built to better understand the

25 interactions between quasi-static stress changes due to mining and the generation of the induced

26 seismicity. Results of this multiparameter approach show a complex rock mass response. We

27 observed two main types of seismic behaviors: one local and temporally short, directly induced by

28 production, the other long-lasting over time and remote from excavations being mainly controlled by

29 geological heterogeneities. In addition to seismicity, we also observed creep-like phenomena

30 induced by mining. In turn, these time-dependent strains appear to be a third mechanism driving

31 seismicity. All these findings underline the importance of considering both seismic and aseismic

32 deformations when one wants to characterize the rock mass response to mining. This significantly

33 enhances our understanding of the phenomena involved, as well as their interactions, for an

34 improved hazard assessment in deep mining operations.

35   Keywords: mining-induced seismicity; rock mass response; creep; quasi-static stress changes;

36 seismic and aseismic deformations; geomechanical numerical modelling

1 Introduction

Anthropogenic seismicity related to underground mining excavations, also referred to as mining-induced seismicity, is one of the most documented types of seismicity caused by human activities. Its characteristics have been largely studied worldwide [1–7], since many decades, with the aim of forecasting its occurrence and mitigate related hazards. Nevertheless, this problem is still far from being solved, especially when massive mining methods are employed at great depths, requiring a deeper characterization of the phenomena involved. In this framework, to be able to fully describe the rock mass response to mining, both seismic and aseismic mechanisms should be investigated. Indeed, as it will be discussed in the following section, mining-induced stresses can result in seismic as well as in aseismic deformations, which both may have significant impacts in terms of rock mass stability and mining strategies.

If mining-seismicity can be monitored by means of seismic networks, aseismic deformations induced by mining can be evaluated by means of geotechnical instruments, such as extensometers or strain measurement cells. Seismic monitoring, which is nowadays a routine technology for seismic hazard assessment in underground mines [8,9], can provide information on large-scale seismic rock mass response when a good coverage of geophones is ensured. On the other hand, geotechnical monitoring is often employed only for local or punctual measurements, not sufficient for describing the aseismic response at large-scale. For this reason, when large-scale geotechnical monitoring is not possible, well calibrated geomechanical numerical models can give an estimation of stress and strain changes due to large-scale mining. There exist nowadays a wide spectrum of modelling approaches and techniques which can be adopted to investigate rock mechanics problems and estimate/simulate rock mass behaviors [10]. Moreover, several studies demonstrate that static and continuous numerical models, although not accounting for rock fractures neither for transient behaviors due to seismic activity (i.e. dynamic models), can be suitable to investigate the potential for induced seismicity in mines [11–14].

These considerations highlight that the coupling between in situ monitoring and geomechanical numerical modelling, could make it possible to better characterize rock mass behaviors in response to mining.

2 Seismic and aseismic deformations in deep mines

When rock mass volumes are extracted due to underground mine excavations the virgin state of stress is disturbed. This results in the redistribution of the local stress field which can lead to seismic and aseismic deformations in surrounding rocks.

The seismic component of the rock mass response is linked with rupture phenomena which emits seismic signals transmitted as elastic waves [15]. Mining-induced seismicity is, thus, the result

71 of fractures propagation inside the rock mass. Depending on fracture dimension and mechanisms

72 involved, mining-induced seismicity can be characterized by microseismic events (M < 2), as well as

73 by much larger events, whose magnitudes can be greater than 3 [16,17].

74 Generally, mining seismicity is directly induced by stress changes due to excavations.

75 Consequently, spatiotemporal behaviors of induced seismicity are directly related to spatial and

76 temporal characteristics of mining operations. Moreover, mining, and in particular the volume of

77 extracted rock mass, also influence the energy content of the resulting induced seismic events [18–

78 20]. The larger the volume mined, the greater the radiated seismic energy.

79 On the other hand, local geological properties can as well influence seismicity in mines. This is

80 the case for the so-called triggered seismicity which is associated with movements along major

81 geological structures. In this case, mining-induced stresses only contribute to the nucleation of the

82 failure, while the rupture process (i.e. events magnitude) is controlled by tectonic or local stress field

83 [21,22]. As a consequence, triggered events can occur at some distance from mine workings and can

84 be characterized by an erratic time distribution [23], as driven by stress changes at larger temporal

85 and spatial scales.

86 Apart from the influence of geology and mining-induced stress, the interaction between

87 subsequent seismic events through static stress transfer has been as well recognized as a mechanism

88 influencing mining seismicity [24,25]. In this case, stress changes induced by larger seismic events

89 strongly affect location and timing of subsequent seismic activity.

90 In addition to seismicity, the rock mass response to mining is also characterized by aseismic

91 mechanisms. Indeed, depending on the rate of stress changes and on rock mass mechanical

92 parameters, slow plastic deformations, not detectable from seismic sensors, can occur. Deformations

93 can have a temporally short behavior, as well as being long-lasting in time. Time-dependent strain

94 (i.e. deformation) is known as creep, a phenomenon observed even in brittle rocks [26]. The primary

95 effect of creep in underground mines is the occurrence of rock deterioration, that is the progressive

96 strength degradation with time [27]. This mechanism mainly affects pillars, as well as roofs, walls and

97 floors of mine galleries, resulting in large deformations which can lead to catastrophic failures under

98 the effect of time [28,29]. A seismic phenomena often observed in relation with creep are repeating

99 earthquakes (also called seismic repeaters), almost identical seismic signals emitted from the same

100 seismic source, which are interpreted as locked seismic asperities (fault patches) loaded by

101 surrounding creep of stable slipping fault plane [30,31]. Such repeaters, are observed in many

102 tectonic regions [32] and in the context of fluid injection for deep geothermal applications [33,34],

103 while they appear rater uncommon and less investigated in the context of mining induced seismicity.

104 Nonetheless, a recent study by Naoi et al. [35] shows the occurrence of small ($-5.1 \leq M_w \leq -3.6$)

105 repeating earthquakes in a deep South African gold mine.

106   The analysis of seismic activity, aseismic deformations as well as of their possible interaction is,
107 then, of paramount importance for a correct interpretation of the rock mass response to mining. In
108 this article, we propose to analyze seismic and aseismic behaviors in Lappberget orebody of
109 Garpenberg mine (Sweden) . Previous studies in the same area of Garpenberg, highlighted a complex
110 rock mass behavior in response to mining. More precisely, De Santis et al. [36] studied
111 spatiotemporal behaviors of seismic clusters in the study area, showing that seismicity can have a
112 local and short-term nature, as well as being long-lasting over time and distant from excavations. In
113 addition, Kinscher et al. [37] showed the occurrence of seismic repeaters in Garpenberg mine,
114 demonstrating that seismicity in the study area is as well driven by aseismic creep. The present paper
115 presents a continuation of the previous works by De Santis et al. [36] and Kinscher et al. [37],
116 investigating seismic and aseismic mechanisms in Garpenberg mine, coupling in situ monitoring data
117 analysis and geomechanical numerical modelling.

3   Study area: Garpenberg mine and Lappberget orebody

119   Garpenberg mine is located in central Sweden and owned by Boliden mining company. Minerals,
120 mainly zinc and silver together with copper, lead and gold as by-products, are extracted from
121 different polymetallic sulfide orebodies, reaching mining depths of about 1300 m. The study area of
122 this article runs between about 1100 m and 1300 m below ground surface, in the block 1250 of
123 Lappberget orebody, the largest and deepest orebody of Garpenberg mine.

3.1   Geological setting and rock properties

125   Lappberget is an almost vertical orebody hosted in a limestone-dolomite unit [38]. Both, the ore
126 and the limestone, are very stiff rocks, with high Young moduli (Table 1). The ore appears to be
127 heterogeneous (Young modulus between 45 and 91 GPa) and characterized by the presence of some
128 weak and very weak zones (Figure 1) mainly constituted by schist rich in talc [39].
129   These zones pose significant issues in terms of mine infrastructure stability. Indeed, rock falls are
130 quite common at drift's faces when they hit a weakness zone. Such failures are particularly observed
131 in the eastern side of the study area, where weak and very weak zones are mostly present (Figure 1).

3.2   Mining method and mining sequence

133   Block 1250 of Lappberget orebody is exploited using the sublevel stoping mining method with
134 backfilling, which ensures a recovery of the ore close to 100%. Stopes are vertical rock columns lying
135 between consecutive drifts along the entire height of the mine (Figure 2), which are subsequently
136 excavated. Stope production is performed level by level, charging and blasting vertical drill-holes.
137 This allows to mine and, then, collect the ore between two overlaying levels, in so-called sub-stopes.

138   This paper focuses on production performed between February 2015 and December 2016, for a
139   total of 52 sub-stopes extracted in the study area (Figure 2). During this period, Stope 13 (in orange
140   in Figure 2) was completely mined along the entire height of block 1250, following a simultaneous
141   bottom-up and top-down sequence. Therefore, the sub-stope between levels 1157 and 1182 (Figure
142   2a) was left as pillar and exploited at the end.

143   3.3   Stress measurements and virgin stress state

144   The stress state in the study area was determined by overcoring method in two different
145   boreholes (H1 and H2) located close to Stope 13 [40]. Results are summarized in Table 2 in terms of
146   principal stress magnitudes, while principal stress orientations are reported in Figure 3.

147   Both measurement points show a strong stress anisotropy, with a sub-vertical minor principal
148   stress (σ_3) and significantly higher horizontal stresses (Table 2). Major (σ_1) and intermediate (σ_2)
149   principal stresses are oriented almost parallel (along Y axis) and perpendicular (along X axis) to mine
150   drifts (Figure 3).

151   None of the measured stress can be assumed to be equal to the virgin stress state, as measures
152   were performed after excavation began. Souley et al. and Tonnellier et al. [41,42] back-computed the
153   virgin stress state (i.e. prior to any excavation) of the study area by means of elasto-plastic numerical
154   modelling, based on stress measurements at H1 and H2 locations. The calculated virgin stress state is
155   reported in Table 3. It was obtained by imposing that the vertical principal stress at depth 1155 m
156   equals the overburden weight. Orientation of principal stresses assumes that σ_1 is parallel to mine
157   drifts (along the Y axis) and that σ_2 is oriented along the X axis, coherently with measurements at H2
158   (Figure 3 on the right). The back-computed virgin stress state is in agreement with the large-scale
159   average Scandinavian stress field, which is characterized by a sub-horizontal σ_1 with mean
160   orientation N120°E ± 45° and generally characterized by a significant anisotropy between principal
161   horizontal stresses and the principal vertical stress [43,44].

162   Magnitudes of measured stresses significantly differ from that of the virgin stress computed by
163   numerical modelling (see Table 2 and Table 3). This indicates that mining excavations strongly
164   influenced vertical as well as horizontal stresses.

165   4   Seismic and aseismic deformation monitoring

166   The study area of this article was instrumented in December 2014 with a monitoring network
167   installed and operated by Ineris (the French national institute for industrial environment and risks).
168   The network consists of both strain cells and seismic sensors for monitoring quasi-static
169   deformations and microseismic activity as excavations progress.

170   Strain cells (named PD and PH) have been installed close to Stope 13, at level 1157 (Figure 4).

171   Both are composed of 12 strains gauges oriented along different directions. Strain measurement are

172   performed on a one-hour basis with an accuracy of about ± 5 µm/m. This allows determining stress

173   changes by inversion, assuming an elastic behavior of the rock.

174   Seismic monitoring network is equipped with six 1-component (1C) and five 3-component (3C)

175   14-Hz geophones installed in such a way that microseismic activity can be recorded within the whole

176   block 1250 (Figure 4). The acquisition system is operating in triggering mode, with an imposed

177   threshold on amplitudes and with a sampling frequency of 8 kHz. Mean location errors are in the

178   order of 15 m within the central area of Lappberget array [45]. For a detailed description of

179   methodologies used for seismic events localization and for seismic source parameters estimation, the

180   reader is referred to [36,45].

5   Geomechanical numerical modelling

181

182   In addition to field monitoring and in order to evaluate strain and stress changes at the scale of

183   the entire block 1250, an elasto-plastic, 3D continuous, mine-wide numerical model has been set up

184   and run using a finite difference code. The numerical model simulates the exact mining sequence

185   followed in block 1250 between February 2015 and December 2016. This corresponds to a total of 52

186   extracted sub-stopes, simulated in 52 equivalent model steps. At each model step, the numerical

187   model estimates quasi-static (i.e. at the equilibrium) strain and stress changes due to mining,

188   discarding short-term temporal effects, such as dynamic loading due to blasting.

5.1   Geometry, discretization, initial and boundary conditions

189

190   The model reproduces the whole Lappberget orebody (Figure 5), which has been constructed in

191   order to be as accurate as possible within the area of interest (i.e. block 1250). Elements considered

192   in the model are the ore, the weak and very weak zones (Figure 5b), as well as mine galleries and

193   stopes within block 1250 (Figure 5a). In addition, shallower mining areas of Lappberget orebody,

194   which extend from – 578 m down to – 1088 m, have also been included in the model (Figure 5 on the

195   left), to account for their influence on the local stress field in block 1250. These areas have been

196   approximated to cuboids whose volume is roughly equal to the excavated rock volume.

197   Model mesh has been built at varying degrees of details, with a high resolution (i.e. a small size)

198   within the area of interest (maximum mesh size of 1 m) and being coarser (i.e. larger) further away

199   (maximum mesh size of 20 m). The final 3D volumetric mesh consists of more than 13.3 million

200   elements.

201   Model boundaries have been placed far enough (about 700 m) from excavations within block

202   1250 to avoid boundary effects, both in horizontal and vertical directions. In addition, null normal

203   displacement conditions were assigned to laterals and lower boundaries.

204   Prior to simulating mining excavations, the model has been consolidated by initializing the load

205   due to the overburden and the virgin stress state. This has been done by introducing the stress

206   gradient reported in Table 3 and already discussed in Section 3.3. Moreover, 14 additional steps are

207   executed in order to: (i) excavate and then backfill with paste the upper levels and (ii) excavate

208   stopes and galleries mined in block 1250 before February 2015, for a total of 13 sub-stopes and a

209   large volume of galleries. Then follow the 52 steps which simulate excavations performed in block

210   1250 between February 2015 and December 2016.

211   **5.2   Constitutive laws and rock mass properties**

212   Geomechanical parameters used for the numerical model are reported in Table 4. The

213   unconfined compressive strength (UCS) of the intact rock, the Hoek-Brown material constant (m_i)

214   and the Geological Strength Index (GSI) were selected for each geological unit, based on rock mass

215   types, structures and discontinuities. The elastic material properties, namely the Young modulus (*E*)

216   and the Poisson ratio (v), were determined choosing mean values from biaxial tests performed on

217   rock samples (Table 1) and paste-fill.

218   Finally, the UCS and m_i values of the intact rock and the GSI values of the rock mass were used

219   to calculate the Hoek-Brown constants *m* and *s* based on the following empirical relations [46]:

$$m = m_i \, exp\left(\frac{GSI - 100}{28 - 14D}\right) \tag{1}$$

220

$$s = exp\left(\frac{GSI - 100}{9 - 3D}\right) \tag{2}$$

221

222   In the previous formulations, we assumed a disturbance factor (*D*) equals to 0 as blasting

223   procedure in Garpenberg is accurately designed and controlled, such that the damage to surrounding

224   rock mass is minimal [46].

225   Assuming that neither thermal, nor hydraulic effects occur, rock masses in the proposed

226   numerical model were modelled assuming purely mechanical constitutive laws. For very stiff rock

227   masses as the orebody in Lappberget, a brittle behavior in the post-failure phase can be expected.

228   According to Hoek and Brown [47], this type of good quality rocks deviate from the elastic behavior

229   for higher stresses compared to soft rocks but, once the peak-stress reached, rock strength

230   decreases dramatically and fractures occur without any prior plastic strain. To model this behavior,

231   Souley et al. [41] developed a non-linear constitutive model which modifies the Hoek and Brown

232   criterion for taking into account the brittle-ductile transition in the post-peak phase. The authors

233   applied the proposed model to the case of Garpenberg mine, showing a significant improvement in

234 the prediction of strain and plastic zone localizations around simulated excavations than a classical
235 Hoek and Brown model. For this reason, in the present study, we adopt the constitutive law
236 proposed by Souley et al. [41] to model the mechanical behavior of the orebody. In contrast,
237 limestone, weak zones and very weak zones, which are softer than the orebody, were modelled
238 considering a perfectly plastic behavior with a Hoek-Brown parabolic failure criterion. Finally, a linear
239 elastic behavior was assumed for the paste. Several tests based on smaller scale models were
240 realized to evaluate mechanical effects of the paste fill. Results show that stress load within the paste
241 directly depends on stope walls (i.e. the ore) convergence: the stiffer the orebody, the smallest the
242 load in the paste fill. For this reason and considering that the orebody in Garpenberg is characterized
243 by stiff properties, the influence of the stress field on the paste could be neglected. This justify the
244 assumption of a linear elastic behavior for the paste, instead of using more complex constitutive
245 models. Moreover, due to the low Young modulus of the paste, the introduction of plasticity would
246 result in computational problems (i.e. bad geometries) due to large strains.

247 **5.3   Defining model outputs at seismic event hypocenters**

248   In order to compare seismic data with geomechanical model outputs, seismic active regions
249 have been selected within the numerical model, based on microseismic events hypocenters. To do
250 so, and in order to account for errors in seismic events localization (on average about 15 m), as well
251 as for numerical model uncertainties, we defined sub-volumes within the whole model, that have the
252 shape of 10 m-radius spheres centered on events hypocenters (Figure 6). The entire selected spheres
253 sub-volume is considered as a new smaller volume of interest with respect to the whole 1250 block.
254 Selecting average or cumulative values of model outputs at each modelling step, it is possible to
255 follow temporal variations of model results within the spheres, looking for differences between
256 seismically quiet and active periods. At the same time, temporal variation of model parameters
257 within the spheres can be compared with that of seismic variables, to look for correlations.

258 **6   Identification of different rock mass responses to mining**

259 **6.1   Overview of observed seismic activity and strain changes**

260   During the analyzed period, more than 750 microseismic events were located around mine
261 galleries in block 1250 (Figure 7a), with moment magnitudes ranging between – 2 and 0.8 [36]. The
262 observed magnitude values are rather small if compared with other hard-rock mines at similar
263 depths [48–50]. No damaging seismic event (e.g. rockbursts) has been observed during the analyzed
264 period, even if some small damage started to be identified within the study area in 2016, when we
265 also observe an overall increase of the seismic rate (Figure 7a).

266   As already pointed out by De Santis et al. [36], two main clusters have been identified during the
267   studied period (Figure 8): the central cluster (CC, in blue in Figure 8) located in the main production
268   area, around Stope 13, and the right cluster (RC, in violet in Figure 8), located in the eastern area of
269   block 1250, in coincidence with the major weak talc-schist zone. Events located outside of these
270   clusters represent only about the 17% of the entire seismicity catalogue (gray dots in Figure 8b and
271   c).

272   The recorded induced seismicity appears to be strongly influenced by mine production, even if
273   microseismic events are more related with blast locations than to blasted volumes [36]. Indeed,
274   throughout the study period, six major seismic sequences have been identified, which are
275   characterized by significant increases of seismicity rate (Figure 7a). Out of six seismic sequences, five
276   are observed in coincidence with the occurrence of production blasts in Stope 13 (Figure 7a, b),
277   during its final mining stages. As reported in Table 5 and in Figure 7a, these blasts are characterized
278   by a wide range of extracted rock mass volumes and blast charges. However, the number of seismic
279   events is not proportional neither to the extracted volumes (Figure 7a and Table 5) nor to the
280   amount of explosive (Table 5), for any of the five seismic sequences directly triggered by excavations.

281   On the other hand, during the same analyzed period, we observe a large number of strain shifts
282   (Figure 9a, b), which are often not accompanied by significant increase of seismic rate. Moreover, of
283   the total 19 strain shifts, 17 are observed in coincidence with the occurrence of production blasts
284   (Figure 9a, b). These observations indicate that strain changes are strongly related to nearby
285   production, where most of the stopes have been extracted inducing mainly aseismic deformations
286   within the surrounding rock masses. However, strain shifts intensity is not proportional neither to the
287   volume of extracted rock mass, nor to the distance from excavations (Table 6).

288   The observed poor proportionality between strain changes and microseismic activity with
289   respect to location and extracted rock mass volumes during blasts, highlights that the rock mass
290   response to mining in the study area is not solely related to the immediate stress change induced by
291   excavations and that additional features influence its pattern.

292   Mechanisms driving seismicity are discussed in detail in the following sections, considering both
293   seismic and aseismic phenomena, and using numerical modelling results as an aid for data
294   interpretation.

6.2   Local seismicity induced by mining

296   Until the beginning of May 2016, the rock mass presents a weak seismic response to mining.
297   Indeed, despite the large number of sub-stopes extracted during this period (34 sub-stopes
298   excavated out of 52 total sub-stopes), the cumulative curve of microseismic events exhibits mainly a
299   constant slope (Figure 7a and Figure 8a). Seismic rate is punctually increased by the occurrence of

some production blasts in Stope 13 (Figure 7a), even if the resulting events are few (see sequences 1, 2 and 3 in Table 5). Seismicity in this first period appears to be mostly a local and temporally short response to nearby production. Indeed, as reported in Figure 8b, events are mainly localized within the CC, thus, in coincidence with the most active production zone. Within the same period, the RC is not very seismically active, with less than 30 events localized in this area (violet dots in Figure 8b).

The local behavior of the rock mass response in this first period is confirmed by the stress redistribution retrieved from numerical modelling. This can be seen in Figure 10, which reports the variation in deviatoric stress (q) between consecutive model steps, namely between steps 10 and 11, which correspond to shift 4 and 5 in Table 6, respectively. The deviatoric stress, or Von Mises equivalent stress, is written as:

$$q = \sqrt{\frac{1}{2}[(\sigma_1 - \sigma_2)^2 + (\sigma_1 - \sigma_3)^2 + (\sigma_3 - \sigma_2)^2]} \tag{4}$$

where σ_1, σ_2, and σ_3 are the major, the intermediate and the minor principal stress, respectively.

Step 11 of the numerical model corresponds with a production blast in Stope 13 (whose location is depicted by a star in Figure 10), which also resulted in seismic sequence 1 (Table 5). Warm colors (from yellow to red) in Figure 10 highlight model zones with Δq > 0, thus, the areas to which stresses are mostly transferred at Step 11 in response to mining in Stope 13. Overall, the excavation presents a radius of influence of about 15 m around the blasted area, indicating that stress transfer acts mainly at local scale.

6.3 Remote seismicity induced by mining

As visible in Figure 8a, the seismic rock mass response is intensified starting from May 2016, when the cumulative curve of microseismic events presents a stepwise trend both for CC and RC, indicating rapid seismic rate changes. During this period, three seismic sequences take place (sequences 4, 5 and 6). Contrary to sequence 4, which is not related to production, the other two are coincident with the last two production blasts in Stope 13 (see Figure 7b). These excavations had the potential, on one hand, to induce an intense seismic activity close to production area (i.e. in the CC) and, on the other hand, to remotely trigger seismicity in the RC, at more than 80 m distance from excavations (Figure 8a and c).

Before the occurrence of seismic sequences 5 and 6, Stope 13 was almost entirely mined and backfilled with paste, leaving only the last two sub-stopes 5 and 6 (see Figure 7b) acting as pillars. Here large stresses are redistributed and concentrated due to the coupled bottom-up and top-down sequence chosen for Stope 13. Indeed, in this zone (indicated by an arrow in Figure 10b), the deviatoric stress computed by numerical modelling reaches more than 60 MPa immediately prior to its excavation, which means an increase of more than 5 times with respect to its initial value.

11

333 Consequently, mining of these final blocks of Stope 13 results in large stress changes. The process of

334 stress redistribution acts, then, at larger scales, influencing the local stress field in the RC area, where

335 seismicity occurs (Figure 8a, c).

6.3.1   *Influence of stress transfer and geological heterogeneities on remote seismicity*

337   To better understand the mechanism of stress transfer toward RC area during sequences 5 and

338 6, we analyzed the temporal evolution of stresses within seismic active regions in the numerical

339 model. This was done by determining mean deviatoric stresses at each model step within the spheres

340 centered at microseismic events hypocenters (see Section 5.3 and Figure 6) and distinguishing

341 spheres belonging to CC from those belonging to RC. Results are reported in Figure 11a and

342 compared with CC and RC seismicity (Figure 11b). Three distinct phases can be identified in Figure

343 11a. At the beginning of the analyzed period (Phase 1), CC and RC regions present similar rates of

344 stress increase. Then, during Phase 2, the mean deviatoric stress remains almost constant within CC

345 at the highest level, while it increases significantly in the RC. Finally, during Phase 3, in coincidence

346 with the two last stages of Stope 13 exploitation, stress in CC drops dramatically until the end of the

347 study period, while stress within RC keeps rising.

348   Phase 1 and 2 are characterized by very low levels of seismic activity within RC, while seismicity

349 is punctually and locally enhanced in CC, due to production in Stope 13 (Figure 11b). Remote

350 seismicity in RC occurs during Phase 3, in coincidence with the destressing of the rock mass in the

351 major production area (i.e. CC). This indicates that, in addition to the large stress release due to final

352 production stages in Stope 13, the remote seismicity within RC is triggered when the CC is not able to

353 sustain large loads, and stresses are preferentially transferred toward the RC area. This is confirmed

354 by the analysis of plastic deformations predicted by numerical modelling within the spheres. Indeed,

355 the percentage of plastic zones with respect to the total number of zones within CC spheres reaches

356 the 39% and the 43% in coincidence with the occurrence of seismic sequences 5 and 6, respectively.

357 On the contrary, during the same seismic sequences, plasticity within RC spheres only represents the

358 9% and the 12% of the total number of zones.

359   In addition to stress transfer, geological characteristics within RC area locally influenced stress

360 field distribution and fracture propagation, as demonstrated by seismic source parameters analysis

361 [36]. Indeed, RC events are characterized by larger stress drops [51], as well as by smaller fracture

362 dimensions, compared to CC seismicity. This trend has been attributed to geological heterogeneities

363 of RC area, where stiff rock masses (i.e. ore and limestone) are interbedded with weak plastic lenses

364 (i.e. talc-schists). As a result, stress in the RC is non-homogeneously distributed and large fractures

365 (i.e. large magnitude events) are impeded by the presence of weak lenses at direct contact with the

366 breaking stiff rock mass (i.e. stiffer lenses).

6.4   Seismicity triggered by aseismic creep

367

368   The occurrence of seismicity driven by aseismic creep in Lappberget orebody has been

369   extensively studied in a recent work by Kinscher et al. [37], who analyzed seismicity of the study area

370   by means of cross correlation cluster analysis looking for the occurrence of multiplet families (i.e.

371   groups of seismic events characterized by highly similar waveforms). The authors demonstrate that

372   more than the half of Lappberget events, within the period 2015-2017, can be classified into

373   different multiplet families with highly coherent (> 0.9) waveform similarity. Families appear to be

374   active over weeks and up to several months and are located both in the CC and in the RC.

375   Observations demonstrate that multiplets found in Lappberget can be interpreted as seismic

376   repeaters, that are the proof of a repeating rupture process of the same seismic source loaded by

377   creep in surrounding areas. Creep in Lappberget is most probably occurring within weak talc-schist

378   lenses which load the interbedded stiff rocks, where seismicity occurs once the induced stress

379   exceeds the point of material failure.

380   Indications of seismicity driven by aseismic creep can be seen in the spatiotemporal behaviors of

381   some seismic sequences analyzed in the present study. Indeed, we identified the occurrence of a

382   seismic sequence not related to mine production (sequence 4). It took place at the beginning of the

383   strong seismic rock mass response period (Figure 8a) and is characterized by events mainly localized

384   within the CC (Figure 12a). One may assume that this sequence was induced by a large magnitude

385   event, through quasi-static stress transfer, in an after-shock like effect. However, no main shock (i.e.

386   larger magnitude event) is observed at the beginning of the sequence (Figure 12b). In addition,

387   sequence 4 (Figure 12b), as well as sequences 2, 3 and 6 (Figure 13), are all characterized by delayed

388   reactivations of seismic rate, which are not driven neither by new blasts, nor by large magnitude

389   events. Seismicity during the observed delayed reactivations do not occurs at same location as the

390   initial activity (e.g. Figure 12a), indicating that a mechanism acting at larger scales is involved. These

391   observations suggest that seismicity is not driven by a cascade-like effect of earthquakes which

392   triggers additional events, thus, a model driven by aseismic slip, as proposed by Kinscher et al. [37],

393   seems to be more appropriate.

6.4.1   Coupling between seismic and aseismic responses

394

395   Creep can be observed in strain measurements (e.g. Figure 9c, d). Indeed, after the sudden

396   strain shift observed in coincidence with blasting, strains do not stabilize quickly in a steady state. A

397   progressive strain drift has been observed for the majority of the recorded strain shifts, indicating

398   that creep (i.e. aseismic slip) is induced by mining. As a result, stress field redistribution and

399   consequent deformations are not immediate but a long-lasting process over time.

400 Moreover, when comparing temporal behaviors of microseismic activity and measured strains,
401 similarities are visible (e.g. Figure 14), implying that seismic activity is decaying proportionally to the
402 decaying rate of induced deformations. This is particularly visible in Figure 14a which reports
403 temporal trends of seismic activity and measured strains at PH cell during seismic sequence 4.
404 Seismicity has a temporal behavior which is nicely reshaping that of measured strains, even for the
405 delayed reactivation which occurs at the same time for seismic activity and measured strains.

406 The observed proportionality between seismicity rate and temporal evolution of measured
407 strains is a strong evidence for the occurrence of coupled mechanisms of seismic and aseismic slip
408 driven by creep, confirming results on seismic repeaters by Kinscher et al. [37]. Indeed, as proposed
409 by other authors [31,33] some faults, or some segments of faults, obey a velocity-strengthening
410 frictional law which leads to a stable silent creep (i.e. slip without seismic activity). Ruptures (i.e.
411 seismicity) occur along locked segments of the faults which are gradually charged by the aseismic
412 creep around them. Once earthquakes are triggered on the seismic parts of the fault, the after-
413 shocks decay rate is driven by creep, thus, seismicity decays proportionally to the slip rate.

6.5 Changes in seismic regime

415 As demonstrated by the occurrence of the non-blast related seismic sequence (sequence 4), and
416 in agreement with findings by Kinscher et al. [37], coupled mechanisms of seismic and aseismic slip
417 appear to be intensified during the period of strong rock mass response to mining, thus, during the
418 final mining stages in Stope 13. This change in seismic regime is also validated by numerical
419 modelling results, particularly when comparing seismic moment (M_0) of microseismic events with the
420 volume of plastic zones computed by modelling. This is shown in Figure 15 which reports M_0
421 cumulated over time for all microseismic events recorded throughout the study period with the
422 volume of plastic zones cumulated between each modelled mining step within spheres sub-volume
423 of the numerical model.

424 Until the occurrence of sequence 4, cumulative curves of seismic moment and plastic volume
425 present similar trends, indicating comparable behaviors of the rock mass response between direct
426 measurements (i.e. recorded seismicity) and numerical model predictions. In other words, model
427 results and observed seismic activity respond similarly to mining excavations in this first analyzed
428 period. As no time-dependent constitutive laws (i.e. creep) have been considered in the numerical
429 model, model outputs variability is solely driven by the quasi-static effect of excavations and by the
430 influence of the modelled geological properties. As a result, the observed similarity between seismic
431 moment and plastic volume trends indicates that seismicity in this first period is mostly driven by
432 quasi-static stress changes induced by mining.

433   On the contrary, in coincidence with sequence 4, seismic moment presents a significant increase

434 which is not followed by an equal increment in plastic volume. Therefore, starting from sequence 4,

435 the two curves show different trends, indicating that numerical model is not anymore capable to

436 account for changes in seismic regime. This means that mechanisms driving seismicity become more

437 complex during the period of strong rock mass response to mining, probably due to the influence of

438 geological characteristics and aseismic creep phenomena.

439   **7   Conclusions and outlooks**

440   In this paper we investigated rock mass behaviors in Garpenberg mine by combining the analysis

441 of geophysical and geotechnical data with geomechanical numerical modelling. Results, which have

442 been interpreted considering mining operations, as well as local geological characteristics,

443 significantly enhanced our understanding of the rock mass response to mining, highlighting complex

444 behaviors. Indeed, at least three concomitant mechanisms appear driving seismicity in Lappberget

445 orebody. On one hand, microseismic activity is directly induced by immediate stress changes due to

446 mining. As a result, seismic events in the central area of the mine (i.e. CC) show strong

447 spatiotemporal correlations with production. On the other hand, seismicity is as well triggered by

448 stress transfer from the main production area (i.e. CC) toward the eastern side (i.e. RC), where local

449 lithological heterogeneities strongly influence seismic activity. As a result, RC seismicity is spatially

450 remote from excavations, even being temporally coincident with blasting, and characterized by

451 significant different source parameters with respect to CC events. Finally, a third overlapping

452 mechanism seems driving seismicity in both CC and RC. It is characterized by a slower response,

453 persistent after the blasts, and responsible for the delayed reactivation of seismic rate observed in

454 most of the analyzed seismic sequences. This latter component of seismicity might be associated to

455 creep-like phenomena induced by mining within soft rocks (i.e. talc-schists), that slowly load

456 surrounding seismic asperities bringing them to rupture (i.e. seismicity).

457   If seismic and aseismic behaviors are generally approached separately with respect to safety

458 issues and hazard assessment in mines, our study demonstrates that time-dependent strains can also

459 be one of the mechanisms driving seismicity. As a result, the aseismic component of the rock mass

460 response to mining should be considered when assessing seismic hazard.

461   Deeper investigations will be needed in order to: (i) better constrain geomechanical and

462 geological origin of seismic repeaters, (ii) characterize and quantify short- and long-term post-blast

463 creep processes in space and time, as well as (iii) their influence on fracture propagation within

464 seismic asperities. This could be done, on one hand, by performing and analyzing local high-

465 resolution strain measurements which could give essential information about transient creep from

466 weak rocks, as well as coseismic strain from repeaters. On the other hand, future seismic data should

be analyzed following the methodology proposed by Kinscher et al. [37] based on template matching techniques, which allow characterizing the nature of seismic repeaters. In addition, dimension and geo-lithological composition of seismic asperities should be examined in future studies by means of drill logs data and geological inspections to be performed in some seismic repeater prone zones. All these data and analyses will be of paramount importance for the conception of an advance geomechanical numerical model able to reproduce mechanisms triggering seismicity at Garpenberg mine. The model should account for (i) the induced seismicity linked with quasi-static stress changes due to mining, (ii) the triggered seismicity due to local geological heterogeneities and stress transfer at large distances and (iii) the seismicity driven be aseismic deformations due to post-blast creep phenomena. A well calibrated geomechanical model representative of the main physical processes involved, combined with improved in situ data analysis, will allow studying aseismic mechanisms at larger scales and constraining the mechanical coupling between creep and seismic ruptures.

Acknowledgements

Bibliography
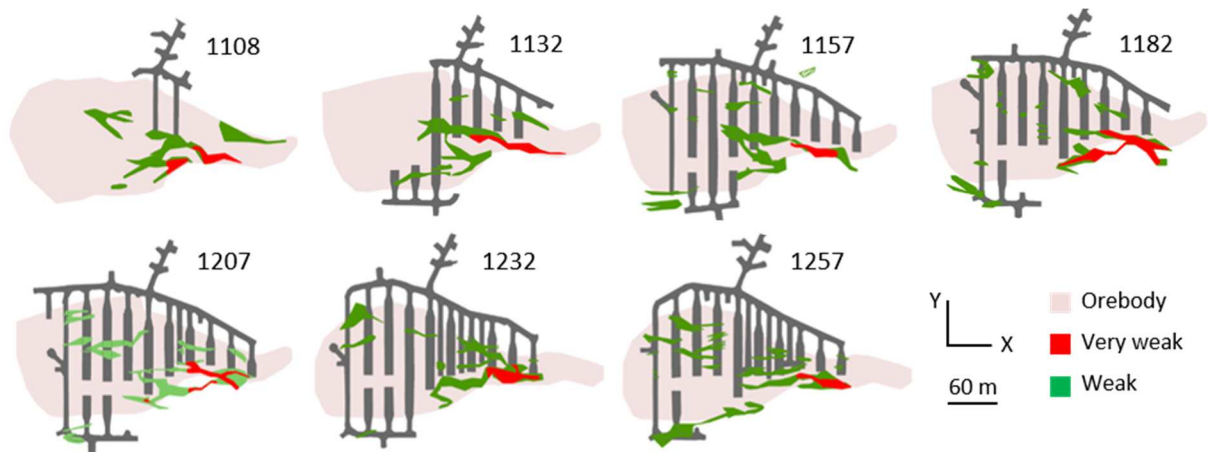
[1] Bischoff M, Cete A, Fritschen R, Meier T. Coal mining induced seismicity in the Ruhr area, Germany. Pure Appl. Geophys. 2010;167:63–75.

[2] Gibowicz SJ. Seismicity induced by mining: Recent research. In: Advances in Geophysics, Elsevier Inc.; 2009. pp. 1–53.

[3] Hudyma M, Potvin Y. Seismic hazard in Western Australian mines. J. South. Afr. Inst. Min. Metall. 2004;104:265–275.

[4] Mendecki AJ. Mine seismology reference book: seismic hazard. Institute of Mine Seismology; 2016.

[5] Mendecki AJ, Van Aswegen G, Mountfort P. A guide to routine seismic monitoring in mines. In: A handbook on rock engineering practice for tabular hard rock mines, Jager AJ and Ryder JA, editors. Cape Town: Creda Communications; 1999. pp. 1-35.

[6] Stec K. Characteristics of seismic activity of the Upper Silesian Coal Basin in Poland. Geophys. J. Int. 2007;168:757–768.

[7] Urbancic TI, Trifu CI. Recent advances in seismic monitoring technology at Canadian mines. J. Appl. Geophys. 2000;45:225–237.

[8] Ge M. Efficient mine microseismic monitoring. Int. J. Coal Geol. 2005;64: 44–56.

500 [9]   Hudyma M, Potvin Y. An engineering approach to seismic risk management in hardrock mines.
501   Rock Mech. Rock Eng. 2010;43:891–906.

502 [10]   Jing L. A review of techniques, advances and outstanding issues in numerical modelling for rock
503   mechanics and rock engineering. Int. J. Rock Mech. Min. Sci. 2003;40:283–353.

504 [11]   Abdul-Wahed MK, Al Heib M, Senfaute G. Mining-induced seismicity: Seismic measurement
505   using multiplet approach and numerical modeling. Int. J. Coal Geol. 2006;66: 137–147.

506 [12]   Shnorhokian S, Mitri HS, Moreau-Verlaan L. Analysis of microseismic cluster locations based on
507   the evolution of mining-induced stresses. In: Proceedings of the 7th International Conference
508   on Deep and High Stress Mining. Sudbury; 14-18 September 2014. p. 709–722.

509 [13]   Spottiswoode SM, Linzer LM, Majiet S. Energy and stiffness of mine models and seismicity. In:
510   Proceedings of the 1st Southern Hemisphere International Rock Mechanics Symposium. Perth;
511   16-19 September 2008. p. 693-707.

512 [14]   Vatcher, McKinnon SD, Sjöberg J. Mine-scale numerical modelling, seismicity and stresses at
513   Kiirunavaara Mine, Sweden. In: Proceedings of the 7th International Conference on Deep and
514   High Stress Mining. Sudbury; 14-18 September 2014. p. 363–376.

515 [15]   Wang H, Ge M. Acoustic emission/microseismic source location analysis for a limestone mine
516   exhibiting high horizontal stresses. Int. J. Rock Mech. Min. Sci. 2008;45720–728.

517 [16]   Alber M, Fritschen R. Rock mechanical analysis of a M_1= 4.0 seismic event induced by mining in
518   the Saar District, Germany. Geophys. J. Int. 2011;186:359–372.

519 [17]   Pechmann JC, Arabasz WJ, Pankow KL, Burlacu R, McCarter MK. Seismological report on the 6
520   August 2007 Crandall Canyon mine collapse in Utah. Seismol. Res. Lett. 2008;79:620–636.

521 [18]   Glowacka E, Kijko A. Continuous evaluation of seismic hazard induced by the deposit extraction
522   in selected coal mines in Poland. Pure Appl. Geophys. 1989;129:523–533.

523 [19]   Kijko A. Theoretical model for a relationship between mining seismicity and excavation area.
524   Acta Geophys. Pol. 1986; 33:231–241.

525 [20]   McGarr A. Seismic moments and volume changes. J. Geophys. Res. 1976;81:1487–1494.

526 [21]   Dahm T, Becker D, Bischoff M, Cesca S, Dost B, Fritschen R, Hainzl S, Klose C, Kühn D, Lasocki S.
527   Recommendation for the discrimination of human-related and natural seismicity. J. Seismol.
528   2013;17:197–202.

529 [22]   McGarr A, Simpson D, Seeber L, Lee W. Case histories of induced and triggered seismicity. Int.
530   Geophys. Ser. 2002;81:647–664.

531 [23]   Gibowicz SJ, Kijko A. An Introduction to Mining Seismology, Academic Press; 1994.

532 [24]   Marsan D, Bean CJ, Steacy S, McCloskey J. Spatio-temporal analysis of stress diffusion in a
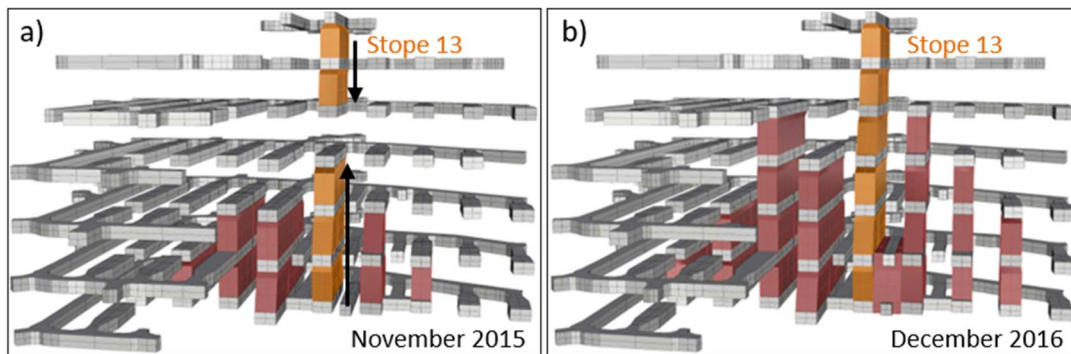533   mining-induced seismicity system. Geophys. Res. Lett. 1999;26:3697–3700.

534   [25] Orlecka-Sikora B, Lasocki S, Lizurek G, Rudziński L. Response of seismic activity in mines to the
535   stress changes due to mining induced strong seismic events. Int. J. Rock Mech. Min. Sci.
536   2012;53:151–158.

537   [26] Scholz CH. Mechanism of creep in brittle rock. J. Geophys. Res. 1968;73:3295–3302.

538   [27] Sainoki A, Mitri HS. Numerical investigation into pillar failure induced by time-dependent skin
539   degradation. Int. J. Min. Sci. Tech. 2017;27:591–597.

540   [28] Alber M. Time dependent properties of sandstones and their effects on mine stability. Solid
541   Earth Discuss. 2013;5:897–916.

542   [29] Kovrizhnykh AM. Deformation and failure of open and underground mine structures under
543   creep. J. Min. Sci. 2009;45:541–550.

544   [30] Linde AT, Gladwin MT, Johnston MJ, Gwyther RL, Bilham RG. A slow earthquake sequence on
545   the San Andreas fault. Nature. 1996;383:65–68.

546   [31] Perfettini H, Avouac JP. Postseismic relaxation driven by brittle creep: A possible mechanism to
547   reconcile geodetic measurements and the decay rate of aftershocks, application to the Chi-Chi
548   earthquake, Taiwan. J. Geophys. Res.: Solid Earth. 2004;109:1–15.

549   [32] Nadeau RM, Johnson LR. Seismological studies at Parkfield VI: Moment release rates and
550   estimates of source parameters for small repeating earthquakes. Bull. Seismol. Soc. Am.
551   1998;88:790–814.

552   [33] Bourouis S, Bernard P. Evidence for coupled seismic and aseismic fault slip during water
553   injection in the geothermal site of Soultz (France), and implications for seismogenic transients.
554   Geophys. J. Int. 2007;169:723–732.

555   [34] Lengliné O, Boubacar M, Schmittbuhl J. Seismicity related to the hydraulic stimulation of GRT1,
556   Rittershoffen, France. Geophys. J. Int. 2017;208:1704–1715.

557   [35] Naoi M, Nakatani M, Igarashi T, Otsuki K, Yabe Y, Kgarume T, Murakami O, Masakale T, Ribeiro
558   L, Ward A. Unexpectedly frequent occurrence of very small repeating earthquakes (- 5.1≤ Mw≤-
559   3.6) in a South African gold mine: Implications for monitoring intraplate faults. J. Geophys. Res.:
560   Solid Earth. 2015;120:8478–8493.

561   [36] De Santis F, Contrucci I, Kinscher J, Bernard P, Renaud V, Gunzburger Y. Impact of geological
562   heterogeneities on induced-seismicity in a deep sublevel stoping mine. Pure Appl. Geophys.
563   2019;176:697–717.

564   [37] Kinscher J, De Santis F, Poita N, Bernard P, Palgunadi K, Contrucci I. Seismic repeaters linked to
565   weak rock-mass creep in deep excavation mining. Geophys. J. Int. 2020. Under publication.

566   [38] Ahmadi O, Juhlin C, Malehmir A, Munck M. High-resolution 2D seismic imaging and forward
567   modeling of a polymetallic sulfide deposit at Garpenberg, central Sweden. Geophysics.
568   2013;78:B339–B350.

569 [39] De Santis F. Rock mass mechanical behavior in deep mines: in situ monitoring and numerical
570   modelling for improving seismic hazard assessment. PhD Thesis. Université de Lorraine, Nancy,
571   France; 2019.

572 [40] Bouffier C, Lahaie F, Bigarré P. Stress measurement campaign and stress monitoring experiment
573   in the Lappberget mining area, at Garpenberg mine, Boliden. Ineris, Technical note DRS-15-
574   127363-05867A, 2015.

575 [41] Souley M, Renaud V, Al Heib M, Bouffier C, Lahaie F, Nyström A. Numerical investigation of the
576   development of the excavation damaged zone around a deep polymetallic ore mine. Int. J. Rock
577   Mech. Min. Sci. 2018;106:165–175.

578 [42] Tonnellier A, Bouffier C, Renaud V, Bigarré P, Mozaffari S, Nyström A, Fjellström P. Integrating
579   microseismic and 3D stress monitoring with numerical modeling to improve ground hazard
580   assessment. In: Proceedings of the 8th International Symposium on Ground Support in Mining
581   and Underground Construction. Luleå; 12-14 September. p. 1-13.

582 [43] Müller B, Zoback ML, Fuchs K, Mastin L, Gregersen S, Pavoni N, Stephansson O, Ljunggren C.
583   Regional patterns of tectonic stress in Europe. J. Geophys. Res.: Solid Earth. 1992;97:11783–
584   11803.

585 [44] Stephansson B, Ljunggren C, Jing L. Stress measurements and tectonic implications for
586   Fennoscandia. Tectonophysics. 1991;189:317–322.

587 [45] De Santis F, Contrucci I, Lizeur A, Tonnellier A, Matrullo E, Bernard P, Nyström A. Numerical
588   approach for evaluating microseismic array performances: case study of a deep metal mine
589   monitoring network. In: Proceedings of the 9th international symposium on rockbursts and
590   seismicity in mines. Santiago; 15-17 November 2017. p.50-57.

591 [46] Hoek E, Carranza-Torres C, Corkum B. Hoek-Brown failure criterion - 2002 edition. In:
592   Proceedings of NARMS-Tac. Toronto; 7-10 July 2002. p.267-273.

593 [47] Hoek E, Brown ET. Practical estimates of rock mass strength. Int. J. Rock Mech. Min. Sci.
594   1997;34:1165–1186.

595 [48] Gibowicz SJ. Scaling relations for seismic events induced by mining. Pure Appl. Geophys.
596   1995;144:191–209.

597 [49] Lizurek G, Rudziński L, Plesiewicz B. Mining induced seismic event on an inactive fault. Acta
598   Geophys. 2015;63:176–200.

599 [50] Nuannin P, Kulhanek O, Persson L, Askemur T. Inverse correlation between induced seismicity
600   and b-value, observed in the Zingruvan Mine, Sweden. Acta Geodyn. Geomater. 2005;2:5–13.

601 [51] Eshelby JD. The determination of the elastic field of an ellipsoidal inclusion, and related
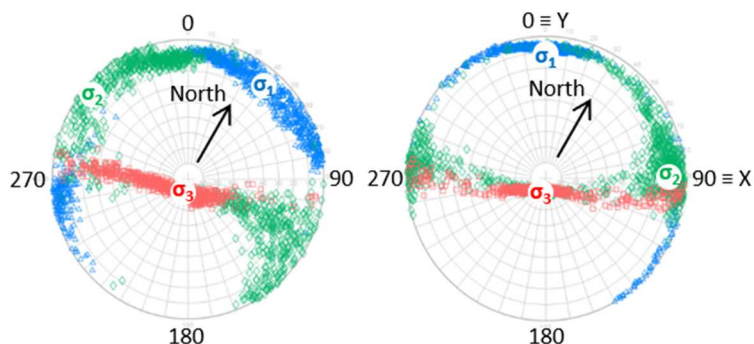602   problems. Proc. R. Soc. London. Ser. A. Mathemat. Phys. Sci. 1957;241:376–396.

603

Figures and figure captions

606   Figure 1 - Orebody, weakness zones and galleries at different depths in block 1250. The figure shows horizontal

607   maps at each of the seven levels of block 1250. Numbers indicate depth (in meters) below ground surface.
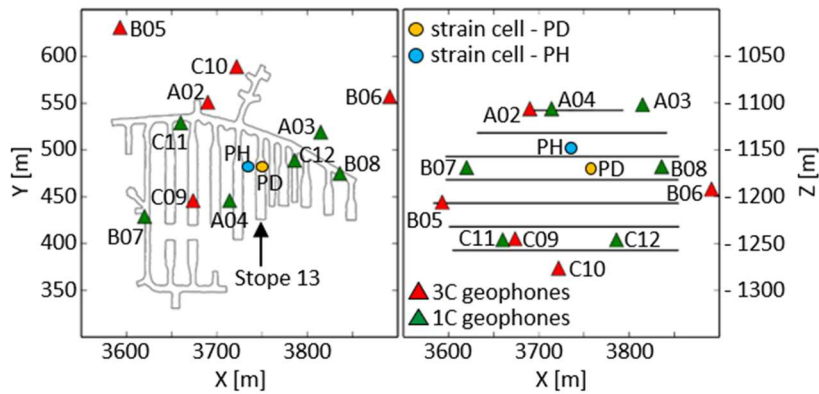

608

609   Figure 2 - Mining sequence in block 1250 of Lappberget. The figure shows how excavation progressed between

610   November 2015 (on the left) and December 2016 (on the right). Red and orange blocks represent excavated

611   sub-stopes. The two arrows illustrate the simultaneous top-down and bottom-up production of Stope 13 (in

612   orange).

613

614   Figure 3 - Stereographic representation of principal stress orientation. H1 measurements are reported on the

615   left, while results for H2 are on the right. Stress orientations are reported with respect to drifts direction (0° ≡ Y

616   axis). True North direction is also depicted in the image (after Bouffier et al., 2015). Note that each data point is
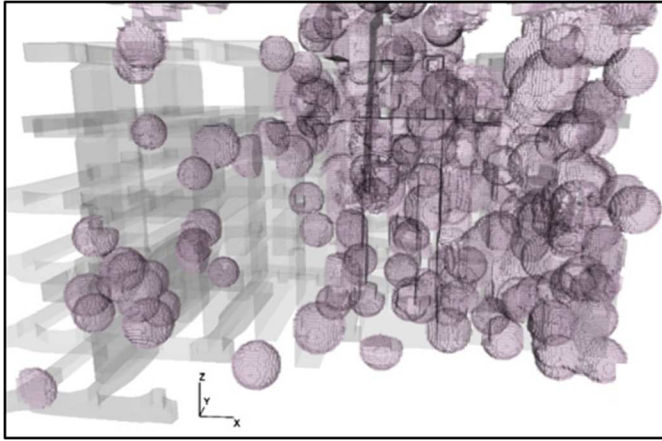
617　the result of an iterative computation which consist in determining all the potential solutions as a function of

618　the errors affecting the estimation. Final solution is that for which the error is minimized.

619

620　Figure 4 - Geophysical and geotechnical monitoring network displayed on a horizontal (left) and a vertical
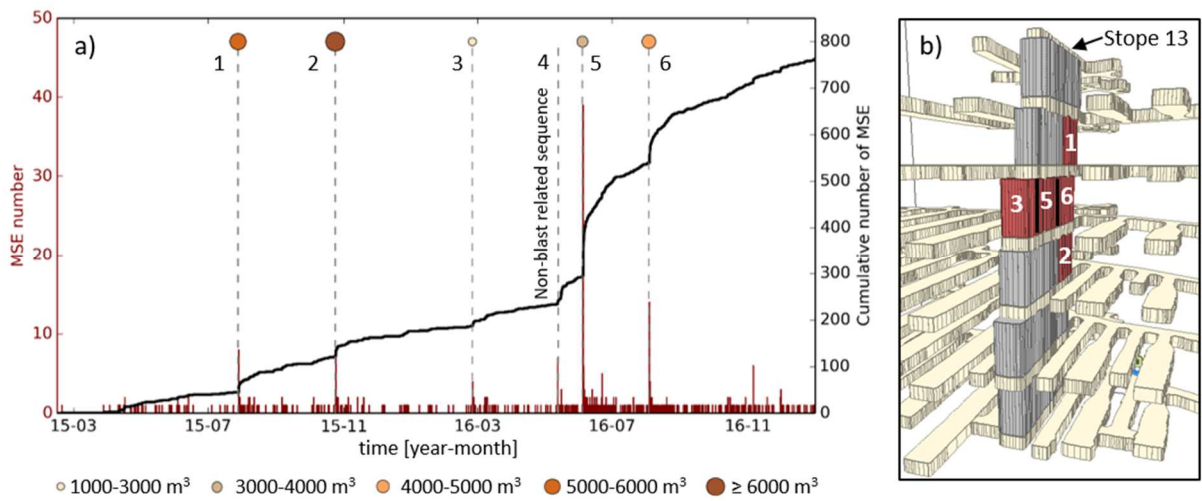
621　(right) cross section of Block 1250.

622

623　Figure 5 - Numerical model geometry. The entire model, together with its boundaries, is reported on the left.

624　The orebody profile is displayed in yellow, while gray areas are assigned to limestone. Upper levels refer to

625　shallower mining areas of Lappberget orebody. Note that, for a better visualization, the limestone surrounding

626　orebody and mined areas has been removed from the left figure. The close-up on the right show the geometry

627　of galleries and stopes in block 1250 (a), as well as that of weak and very weak zones (b) in green and red,
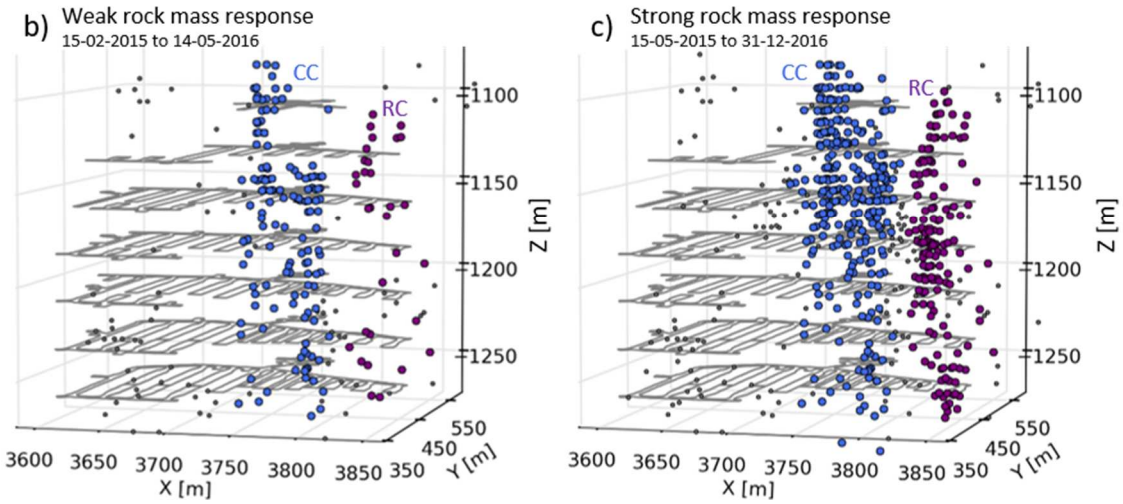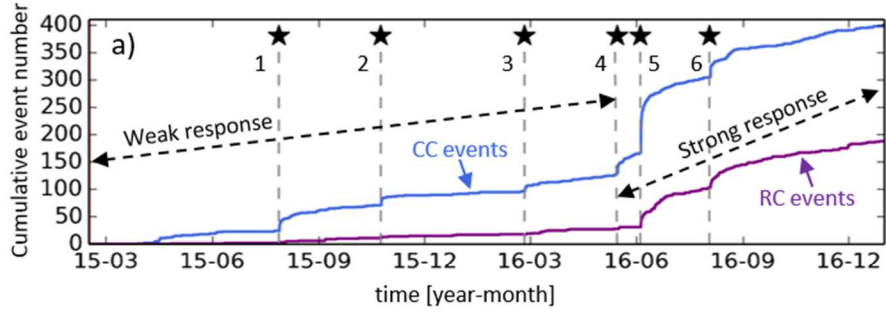
628　respectively.

629

Figure 6 - Selection of seismic active regions within the numerical model. This sub-volume is identified by 10 m-radius spheres centered at microseismic events hypocenters. Grey areas represent galleries and stopes in block 1250, as built in the numerical model.
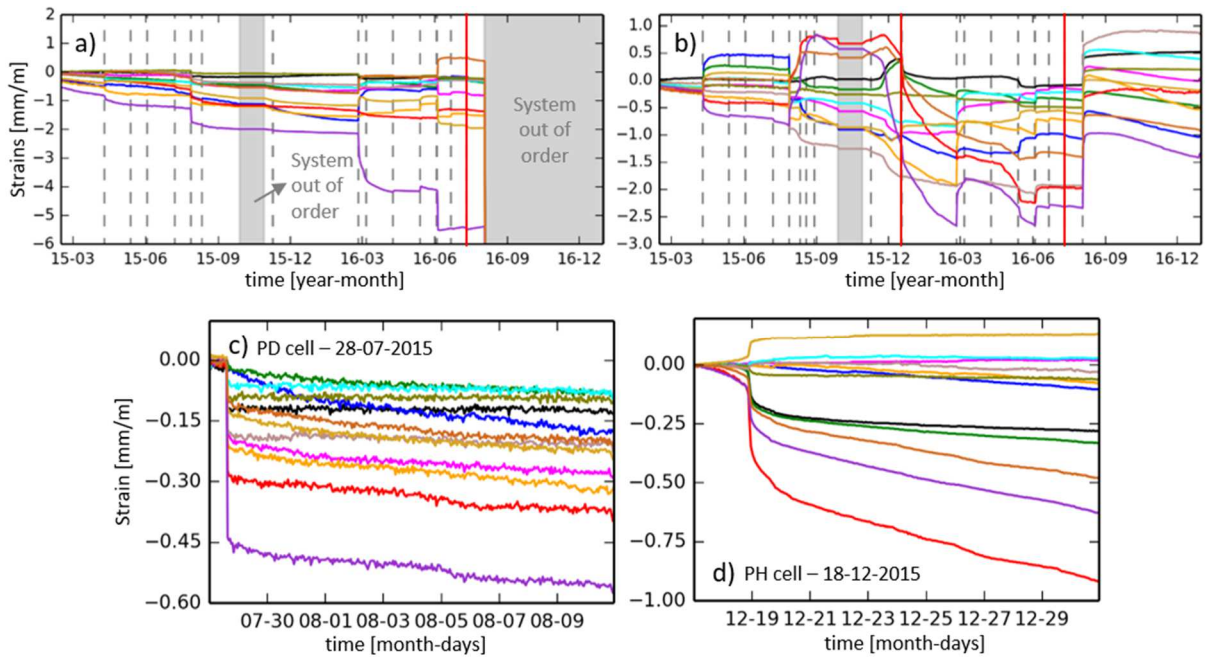

633

Figure 7 - Microseismic activity and production blasts. (a) Number of microseismic events (MSE) per hour (in red) and cumulative number of events (in black). Dashed lines indicate the occurrence of some seismic sequences. Production blasts which triggered the seismic sequences are reported by circles colored and sized according to the volume of extracted rock mass. (b) Positions of mined sub-stopes (in red) in Stope 13 during seismic sequences 1, 2, 3, 5 and 6. Gray blocs indicate sub-stopes mined and refilled with paste.
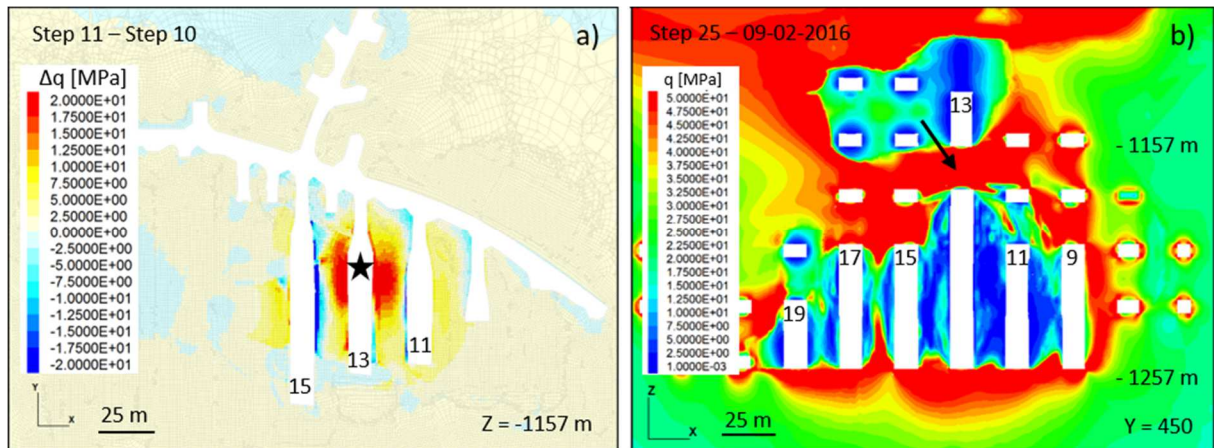
639

640

641 Figure 8 - Space-time characteristics of microseismic activity. (a) Cumulative number of microseismic events

642 separated between Central Cluster (CC) and Right Cluster (RC). Stars and dashed lines indicate seismic

643 sequences numbered as in Figure 7. (b) Localization of microseismic events during the period of weak rock

644 mass response. Gray dots indicate events located outside CC and RC. (c) The same as in (b) but for the period of

645 strong rock mass response to mining.

646

647 Figure 9 - Strain measurements at PD (a) and PH (b) cells over the whole analyzed period and during two
648 different strain shifts induced by production blasts (c and d). Colored lines in the figures represent the measure
649 at each gauge of the cells. Dashed gray lines in (a) and (b) indicate significative strain changes occurred in
650 coincidence with production blasts. Red lines in (a) and (b) refer to strain changes non-related to production.
651 Gray areas in (a) and (b) highlight periods where the system was out of order.
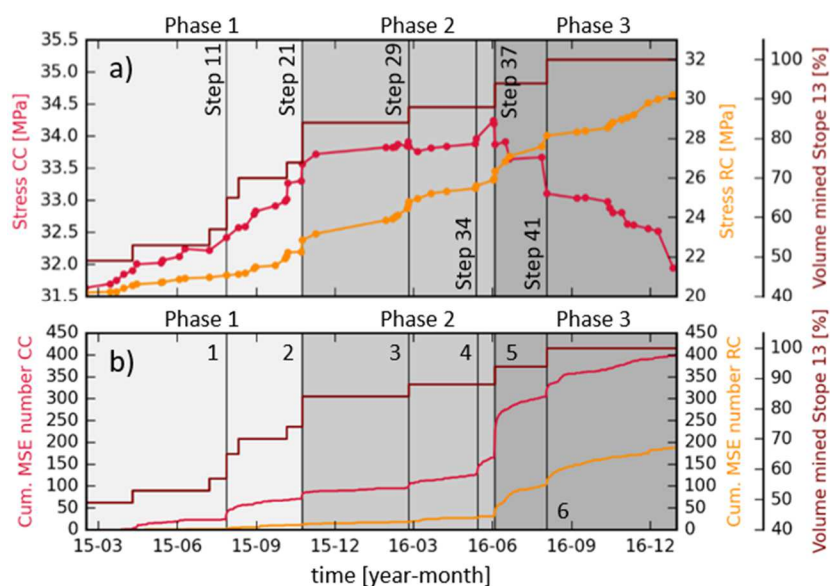
652

653
654 Figure 10 - Stress changes retrieved by numerical modelling. (a) Difference in deviatoric stress between
655 subsequent model steps along a horizontal section in block 1250. The star indicates the position of the
656 production blast at model Step 11. (b) Contour of deviatoric stress along a vertical section for the Step 25 of the
657 numerical model. The arrow highlights the last exploited area in Stope 13. White areas in (a) and (b) depict
658 mined stopes and galleries. Numbers within white areas indicate stope's names, while numbers on the right of
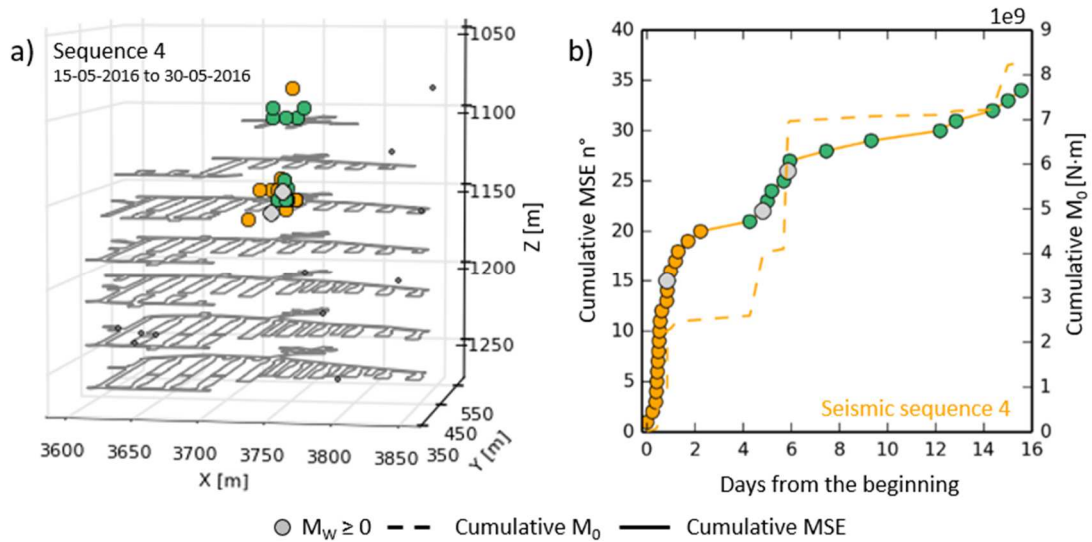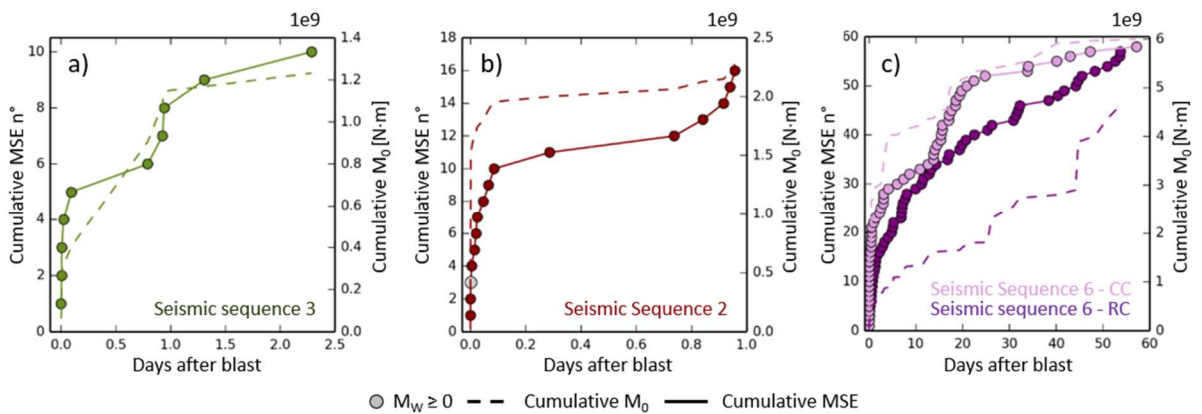659 figure (b) refer to depths.

660

661
662 Figure 11 - Temporal trend of stress state in seismogenic regions retrieved by numerical modelling (a)
663 compared with temporal trend of microseismic activity (b). (a) Average deviatoric stress at each model step

24

664 within CC (in red) and RC spheres (in yellow). (b) Cumulative number of microseismic events in CC (in red) and

665 RC (in yellow). The brown curve in (a) and (b) reports the percentage of excavation advancement in Stope 13.

666 Vertical lines indicate the occurrence of a seismic sequence (in b) and the corresponding numerical model step
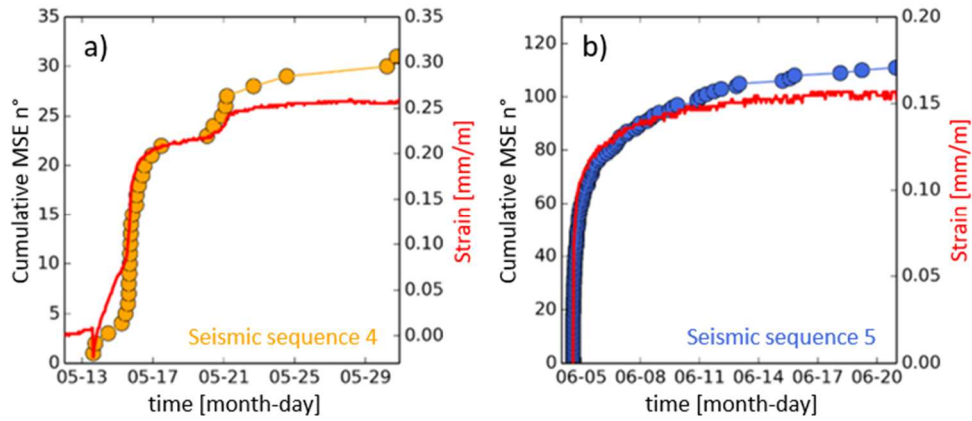
667 (in a).

668

669 Figure 12 - Spatiotemporal characteristics of seismic sequence 4. (a) Localization of microseismic events during

670 sequence 4, analyzed along 16 days. (b) Cumulative number of microseismic events (MSE) (left-hand axis) and

671 cumulative seismic moment (M_0) (right-hand axis) over 16 days. Yellow dots in (a) and (b) indicate events

672 occurred at the beginning of the sequence, while green dots are the events occurred during the reactivation of

673 the sequence.

674

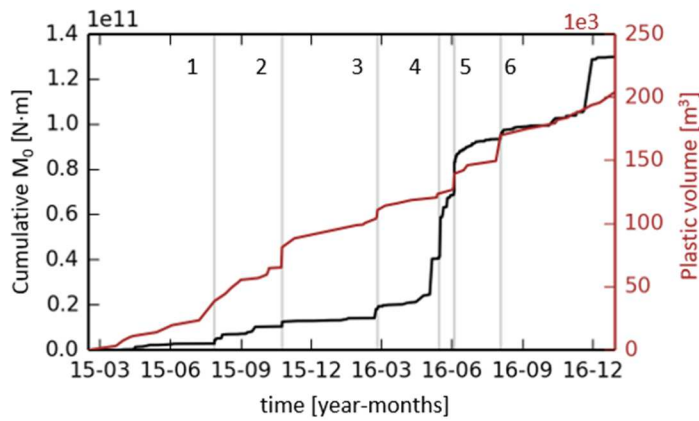675 Figure 13 - Temporal trend of some seismic sequences. The charts report the cumulative number of

676 microseismic events (left-hand axis) and the cumulative seismic moment (right-hand axis) during sequence 2

677 (b), sequence 3 (a) and sequence 6 (c). For this latter, events are reported separately for central cluster (CC)

678 and right cluster (RC). Note that temporal intervals are different per each sequence.

679

680

681 Figure 14 - Comparison between seismicity and strain measurements. (a) Cumulative number of microseismic

682 events (left-hand axis) during seismic sequence 4 and measured strains (right-hand axis) at PH cell in the same

683 temporal interval. (b) The same as in (a), but during seismic sequence 5 and considering strains measured at PD

684 cell.

685

686 Figure 15 - Comparison between cumulative seismic moment (M_0) (in black) and cumulative plastic volume

687 retrieved by numerical model (in red). Plastic volume is computed considering only model zones within the

688 spheres sub-volume as defined in Figure 6. Gray lines indicate seismic sequences occurrence.

Tables and tables captions

Table 1 - Rock geomechanical properties retrieved from biaxial tests on rock samples.

Depth [m]	Lithology	Young modulus [GPa]	Poisson ratio	Density [kg/m3]	UCS[2] [MPa]	References
- 1155	Ore	44.9	0.23	30301	150	Bouffier et al. (2015)
		64.1	0.23			
- 852	Ore	84.7	0.15	3331	196	
		90.7	0.15	3270	146	van Koppen (2008)
- 883	Limestone	55	0.17	2714	73	
- 967		60	0.12	2722	100	

[1]Average density resulting from three laboratory tests; [2]Unconfined compressive strength.

Table 2 - Magnitudes of measured principal stresses obtained by using the overcoring method.

Sample	Depth [m]	σ1 [MPa]	σ2 [MPa]	σ3 [MPa]	References
H1	- 1155	57	46	26	Bouffier et al. (2015)
H2	- 1155	56	40	28	

Table 3 - Computed virgin stress state at level -1155 m and vertical stress gradients [41].

Initial stress state at level 1155 [MPa]		Vertical stress gradient [MPa/m]	
σ1 (σyy)	47.3	gH/y	0.041
σ2 (σxx)	44.4	gh/x	0.038
σ3 (σzz)	34.3	gv/z	0.030

Table 4 - Geomechanical parameters retained for numerical modelling.

Materials	UCS1 [MPa]	mi	GSI2	E [GPa]	v	m	s
Ore	188	20	80	66	0.2	10	0.112
Limestone	110	20	80	57	0.18	10	0.112
Weak	30	9	38	20	0.3	1.0	0.001
Very weak	10	9	25	2	0.4	0.63	0.00024
Pastefill	-	-	-	0.5	0.2	-	-

[1]Unconfined compressive strength; [2]Geological Strength Index.

Table 5 - Seismic sequences and production blasts characteristics.

Seismic sequence	Date	Rock volume [m3]	Blast charge [kg]	Number of MSE in 24h
1	28-07-2015	5330	6669	17
2	24-10-2015	6702	5473	15
3	25-02-2015	2758	2963	8
4	15-05-2016	-	-	15
5	04-06-2016	3978	6597	94
6	03-08-2016	4346	4527	38

Table 6 - Characteristics of strain shifts and related production blasts. The column Stope reports the sub-stope blasted during each shift. First number refers to stope's name, second to mining level, while the third reports the number of the sub-stope exploited at the

corresponding level. Distances are computed from strains cells to the centroid of blasted volumes.

Shift	Time	Max. strain PD|PH [μm/m]	Stope	Explosive [kg] | volume [m3]	Distance PD|PH [m]
1	10-04-2015	100 | 411	13_1157 #1	3553 | 2239	40 | 37
2	13-05-2015	20 | 30	15_1232 #1	4302 | 3970	92 | 97
3	03-06-2015	15 | -12	15_1232 #2	6444 | 3724	78 | 71
4	08-07-2015	-74 | -53	13_1157 #2	4212 | 2910	31 | 27
5	28-07-2015	-449 | -654	13_1157 #3	6669 | 5330	22 | 15
6	11-08-2015	50 | 325	13_1207 #1	4172 | 3275	57 | 64
7	19-08-2015	- | 38	11_1232 #1	4152 | 2807	- | 73
8	29-08-2015	- | 34	11_1232 #2	4781| 3534	- | 65
9	09-11-2015	-18 | -14	15_1257 #2	4177| 4563	91 | 82
10	18-12-2015	- | -320	13_1157	105 | -	- | 10
11	25-02-2016	600 | 635	13_1182 #1	2963 | 2758	39 | 43
12	06-03-2016	33 | 62	11_1207 #2	4827 | 5503	45 | 57
13	09-04-2016	68 | 23	17_1207 #1	3440 | 2527	80 | 81
14	13-05-2016	142 | 40	17_1207 #2	- | 6497	66 | 67
15	03-06-2016	42 | 29	15_1207 #2	5544 | 4345	82 | 79
16	04-06-2016	-1181 | 142	13_1182 #2	6597 | 3978	27 | 32
17	21-06-2016	98 | 53	15_1207 #2	6766 | 7078	55 | 59
18	11-07-2016	34 | 77	-	-	-
19	03-08-2016	- | 2561	13_1182 #3	4527 | 4346	- | 18